

# Geophysical Research Letters



## RESEARCH LETTER

10.1029/2021GL093026

### Key Points:

- Core Co1401 from Lake Levinson-Lessing is with a length of 46 m, an exceptional lacustrine sediment record in the Russian Arctic
- Core Co1401 provides sediments with unusual homogenic magnetic mineralogy and mineral magnetic properties
- Lake Levinson-Lessing is expected to become a key record of paleomagnetic research on the Eurasian tangent cylinder

### Supporting Information:

Supporting Information may be found in the online version of this article.

### Correspondence to:

S. Scheidt,  
[stephanie.scheidt@uni-koeln.de](mailto:stephanie.scheidt@uni-koeln.de)

### Citation:

Scheidt, S., Egli, R., Lenz, M., Rolf, C., Fabian, K., & Melles, M. (2021). Mineral magnetic characterization of high-latitude sediments from Lake Levinson-Lessing, Siberia. *Geophysical Research Letters*, 48, e2021GL093026. <https://doi.org/10.1029/2021GL093026>







Received 18 FEB 2021

Accepted 29 APR 2021

© 2021. The Authors.

This is an open access article under the terms of the [Creative Commons Attribution License](#), which permits use, distribution and reproduction in any medium, provided the original work is properly cited.

## Mineral Magnetic Characterization of High-Latitude Sediments From Lake Levinson-Lessing, Siberia

Stephanie Scheidt<sup>1</sup> , Ramon Egli<sup>2</sup> , Matthias Lenz<sup>1</sup> , Christian Rolf<sup>3</sup> , Karl Fabian<sup>4,5</sup> , and Martin Melles<sup>1</sup> 

<sup>1</sup>Institute of Geology and Mineralogy, University of Cologne, Cologne, Germany, <sup>2</sup>Central Institute for Meteorology and Geo-dynamics (ZAMG), Vienna, Austria, <sup>3</sup>Leibniz Institute for Applied Geophysics (LIAG), Hannover, Germany, <sup>4</sup>Geological Survey of Norway (NGU), Trondheim, Norway, <sup>5</sup>Department of Geoscience and Petroleum, Norwegian University of Science and Technology, Trondheim, Norway

**Abstract** Levinson-Lessing Lake in northern Central Siberia is a sedimentary archive characterized by continuous, widely constant sedimentation at high rates (0.7 m ka<sup>-1</sup> for >32 ka). This study provides the first evidence of the suitability of the lake's sediments for paleomagnetic analyses using the 46-m-long core Co1401. Although the lowermost 8 m are disturbed, the upper 38 m of Co1401 provide the preconditions for an exceptional, high-resolution paleomagnetic record located within the tangent cylinder of the inner core. High-resolution analyses of magnetic susceptibility, anhysteretic remanent magnetization, isothermal remanent magnetization, and hysteresis parameters show largely uniform mineral magnetic properties. First-order reversal curves indicate magnetite particles in pseudo-single domain state are the main remanence carrier, supplemented by single-domain particles, originating likely from magnetotactic bacteria. Above 6.7 m, the bulk magnetic mineralogy is slightly harder than below and initial greigite formation occurs. However, the main remanence carriers are still of detrital origin.

**Plain Language Summary** Levinson-Lessing Lake in northern Central Siberia is a sedimentary archive characterized by continuous, widely constant sedimentation at high rates (0.7 m ka<sup>-1</sup> for >32 ka). Because lakes with such long-term constant properties are extremely rare throughout the Arctic Circle, the 46-m-long sediment core Co1401 recovered in 2017 provides an exceptional archive for climate and environmental changes of the past, but also for recordings of the evolution of the Earth's magnetic field (EMF) in this region. This study tested the suitability of Co1401 for paleomagnetic analyses using hundreds of samples and various analytical approaches. Although the lowermost 8 m are shown to be disturbed, the upper 38 m of Co1401 provide an unusual homogeneous mineral-magnetic composition and properties. In the uppermost 6.7 m, the magnetic mineralogy is slightly different with greigite as additional component. The presence of this mineral can be a problem in paleomagnetic studies, as it overprints the primary information recorded in the archive. In this case, the formation is only initial and thus not an issue. Overall, Co1401 provide ideal preconditions for a paleomagnetic archive. Thus, an upcoming paleomagnetic-based chronology will unlock this archive for future studies on paleoclimate, paleoenvironment, and the evolution of the EMF.

## 1. Introduction

Most of the Arctic lies inside the tangent cylinder of the inner core (>69.5°N) and thus dominantly records magnetic fields generated by convection in the northern magneto-hydrodynamically closed compartment of the outer core. These fields are decoupled and probably behave partly independent from the global secular variation (St-Onge & Stoner, 2011). Our understanding of the interplay between dipolar and non-dipolar components of the Earth's magnetic field (EMF) can be improved by analyzing records from sedimentary archives. Yet, most Arctic Ocean records have low temporal resolution and are also biased by diagenetic processes coupled to water depth and climatic conditions (Wiers et al., 2019, 2020). On the other hand, terrestrial records extending back beyond the Last Glacial Maximum are exceptionally rare throughout the complete Arctic Circle. Therefore, observation-based reconstructions of the evolution of features, such as the Siberian flux lobe (Figure 1a), are so far not possible in the Eurasian Arctic. Levinson-Lessing Lake in the Russian Arctic is best suited for providing a long-range high-resolution record. It is the deepest lake at the Taymyr Peninsula, following a tectonic trench that was reshaped by glacial erosion during early

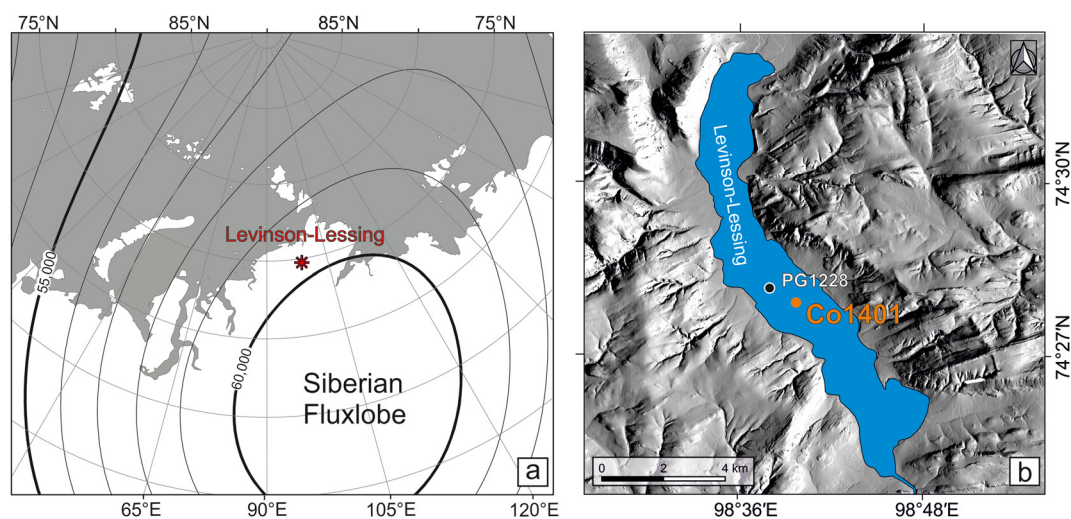


**Figure 1.** Location of the Levinson-Lessing Lake in Siberia and of the drill sites. (a) Present geomagnetic field intensity over Siberia (field lines in nT) and location of Levinson-Lessing Lake on the Taymyr Peninsula (b) Coring sites Co1401 (74°27′54″N, 98°39′58″E) and PG1228.

Weichselian (Niessen et al., 1999). Its sedimentary record is a target for paleoenvironmental and paleoclimatic studies since the 1990s. First coring in 1995 provided a ~22-m-long sediment core (PG1228) that revealed a continuous, rather constant, and high sediment accumulation ( $\sim 0.70 \text{ m ka}^{-1}$ ) throughout the last ~32 ka (Andreev et al., 2003; Ebel et al., 1999). Seismic surveys presented the prospect of up to 115 m of undisturbed sediments (Lebas et al., 2019).

In 2017, a new 46-m-long sediment core (Co1401) was recovered by the Russian-German project PLOT (Paleolimnological Transect) close to PG1228 (Figure 1b; Text S1). Because paleomagnetic measurements have not been performed, the usability of Co1401 for paleointensity estimations was first tested with whole-core measurements; then, high-resolution discrete samples were taken. This study discusses the whole-core measurements and further mineral magnetic investigations, as a first step towards unlocking an exceptional sedimentary archive that has the potential to become a paleomagnetic key archive for the Eurasian Arctic. Comparable study sites are not available within a radius of  $>1,500 \text{ km}$ .

## 2. Materials and Methods

### 2.1. Core Description

The composite core Co1401 has a cumulative length of 45.95 m and gaps of 2–36 cm between the 24 core sections (Text S1). The sediment record consists of hemipelagic silty sediments irregularly interrupted by turbidites, reflecting pseudo-continuous event-based sedimentation. The turbidites are up to 8 cm thick and show fining upward of grain size with fine sand as maxima at the base. However, most turbidites are much thinner than 1 cm and composed from fine sand and silt. The total organic carbon content (Text S2) is generally low (0.6%–3.7%) with highest values restricted to the uppermost ~7m correlated depth (mcd, Figure 2). Above 38 mcd, most of the sediment sequence is finely laminated without signs of deformation or bioturbation. Below 38 mcd, in contrast, no lamination is visible, and the consistency is significantly softer than above.

### 2.2. Whole-Core Measurements and Sample Preparation

Whole-core measurements of magnetic susceptibility ( $\kappa_{\text{rel}}$ ) were performed with a loop sensor (Magnon VFSM susceptibility bridge). The natural remanent magnetization (NRM), and the remanence after alternating field (AF) demagnetization were measured using a 2G 760R-SRM (Text S2). Afterward, the cores were split lengthwise and geochemical and sedimentological analyses were performed. Gaps caused by core loss or gas expansion were closed by upward displacement of the remaining sediment. For further magnetic

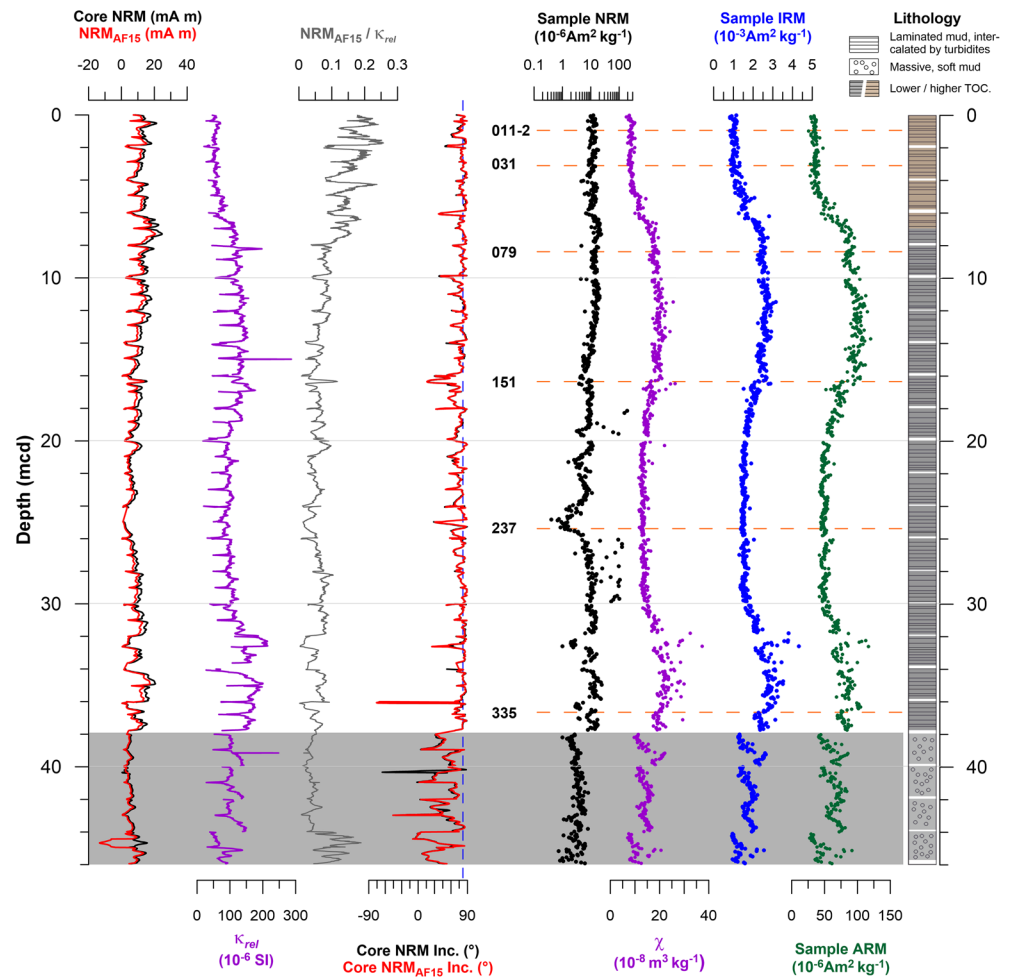


**Figure 2.** Lithology and downcore plots of magnetic properties. Results of whole-core measurements (left): natural remanent magnetization (NRM),  $NRM_{AF15}$ ,  $\kappa_{rel}$ , NRM Inclination (NRM Inc.),  $NRM_{AF15}$  Inc. The blue vertical dashed line marks the  $82.1^\circ$  inclination expected for a geocentric axial dipole. Discrete sample measurement results (right): NRM,  $\chi$ , isothermal remanent magnetization (IRM), anhysteretic remanent magnetization (ARM). Note the logarithmic scale for NRM. Samples shown in Figure 4 are marked by orange horizontal dashed lines. Gray background  $>38$  mcd.

analyses, 903 samples in  $6 \text{ cm}^3$  plastic boxes were sampled. In addition, 124 gel-capsule samples and six magnetic extracts (Text S3) were prepared.

### 2.3. Discrete Sample Measurements

The NRM, anhysteretic remanent magnetization (ARM), and isothermal remanent magnetization (IRM) were measured for all 903 samples using a 2G Enterprises SQUID SRM and subsequently stepwise AF demagnetized (Text S4). The temperature dependent magnetic susceptibility  $\kappa(T)$  was determined for six samples using an Agico MFK2 (Text S3).

The hysteresis and backfield curves of 124 gel-capsular samples were measured using a Lakeshore 8604 VSM, following the protocol described in Fabian (2003). Saturation magnetization ( $M_s$ ) and high-field susceptibility ( $\chi_{hf}$ ) were calculated from hysteresis data using the approach to saturation model of Fabian (2006), while the saturation remanence ( $M_{rs}$ ) and coercive force ( $H_c$ ) were obtained from the crossing points of hysteresis with the magnetization and field axes, respectively. The coercivity of remanence ( $H_{cr}$ ) was determined from the backfield of remanence curve by linear interpolation. Five to six identical high-resolution first-order reversal curve (FORC) measurements (Pike et al., 1999) were performed for six representative samples. FORC data were stacked and processed using the VariForc software (Egli, 2013).

Coercivity distributions were obtained from the processed data according to Egli and Winklhofer (2014) and analyzed as described in Egli et al. (2010). See Text S5 for further details about VSM measurements.

### 3. Results and Discussion

#### 3.1. Downcore Magnetic Properties

Below 38 mcd, the magnetic susceptibility ( $\kappa_{\text{rel}}$ ) and inclinations determined by whole core measurements, as well as the mass-specific susceptibility ( $\chi$ ), ARM, and IRM values of discrete samples, show the low values of the uppermost core meters at the top and transition to higher values toward the bottom (Figure 2). This observation, along with the lack of stratification and soft consistency, strongly argues for disturbance of the sediments during coring operation. It seems that the core chambers erroneously collected sediment on its way to coring depth. Results from measurements below 38 m are, therefore, not further discussed.

Above 38 mcd, the whole-core measurements of  $\kappa_{\text{rel}}$ , NRM, and the remanence remaining after 15 mT AF demagnetization ( $\text{NRM}_{\text{AF15}}$ ) furthermore show a systematic drop at the ends of core sections, which results from the  $\sim 10$  cm wide response functions of the measuring devices. For the same reason, the signal is smoothed within core sections. Nevertheless, limited NRM variations along the core axis ( $2.5\text{--}24.7$  mA m $^{-1}$ ) suggest a quite homogeneous recording efficiency. The differences between the NRM and the  $\text{NRM}_{\text{AF15}}$  are marginal and suggest a small amount of viscous magnetized particles. Compared to the NRM,  $\kappa_{\text{rel}}$  exhibits larger fluctuations and shows large-amplitude variations. A whole-core relative paleointensity (RPI) has been calculated using the ratio  $\text{NRM}_{\text{AF15}}$  and  $\kappa_{\text{rel}}$ . Hereby, it is assumed that the response functions of the two measurement devices do not differ widely. Apart from the uppermost 7 m, the whole-core RPI shows only minor fluctuations. This result can be explained by a relative homogenous magnetic mineralogy. The whole-core inclinations measured before and after 15 mT AF demagnetization are very similar. Shallowest inclinations coincide frequently with core section ends. This is a known phenomenon and most likely due to the compression of the core ends during transport. The overall mean inclination of  $82.1^\circ$  coincides with the value expected by a geocentric axial dipole (GAD). These results suggest that Co1401 is suited for further paleomagnetic studies.

The NRM values obtained from discrete samples show a much higher variability than those of whole-core measurements. Since the strongest NRM fluctuations occur in sections where the concentration-dependent parameters  $\chi$ , ARM, and IRM are stable, the lower remanences may have been acquired during periods of a weak EMF. The logarithmic scale necessary to plot all NRM values in Figure 2 prevents large amplitude variations from being detected. However, the trend is as for  $\chi$ , ARM, and IRM with higher values between  $\sim 7\text{--}17$  mcd and  $\sim 32\text{--}38$  mcd. Because previous studies suggested the Pleistocene-Holocene transition to be at about 7 m (Andreev et al., 2003; Ebel et al., 1999), the change in  $\sim 7$  mcd depth in Co1401 is likely related to climatic and environmental changes (Andreev et al., 2003). The ranges of whole-core NRM,  $\kappa_{\text{rel}}$ , NRM,  $\chi$ , ARM, and IRM with respect to depth level are given in Table S1.

#### 3.2. Magnetic Mineralogy and Magnetic Granulometry

The hysteresis loops are similarly shaped for all samples (Figure S1). Hysteresis parameters from 38 to  $\sim 6.7$  mcd and from 6.7 mcd to the top form two slightly overlapping clusters in the pseudo-single-domain (PSD) range of the Day plot (Day et al., 1977; Figure 3a). Tight clustering of hysteresis parameters in the lower of these sections, along with the stable values of  $H_c$  and  $H_{cr}$  (Figure 3b) suggest a consistent magnetic mineralogy. The ratio of the energy  $\Delta E$  enclosed between the  $M_{\text{sl}}(B)$  curve and the upper branch of hysteresis, and the energy  $E_{\text{hys}}$  of the whole hysteresis indicate low proportions of multi-domain (MD) particles larger  $\sim 5$   $\mu\text{m}$  in this depth range (Fabian, 2003). Thus,  $\Delta E/E_{\text{hys}}$  confirm the PSD indication in the Day plot by excluding mixtures of single-domain (SD) and MD particles. The differentiation of the sections above and below 6.7 mcd is also evident from the  $\kappa(T)$  measurements (Figures 3c and S2). However, all measurements show a major decrease in susceptibility at about  $\sim 585^\circ\text{C}$ , the Curie temperature of magnetite. The moderate decrease between  $\sim 320^\circ\text{C}$  and  $585^\circ\text{C}$  may be determined by Ti-magnetite, which show a wide range of Curie temperatures depending on composition and oxidation state (Nishitani & Kono, 1983). However, the heating curve also resemble that of natural maghemite (Gehring et al., 2009), a mineral formed by low-temperature oxidation of magnetite and in soil-formation processes (Liu et al., 2010). Especially the

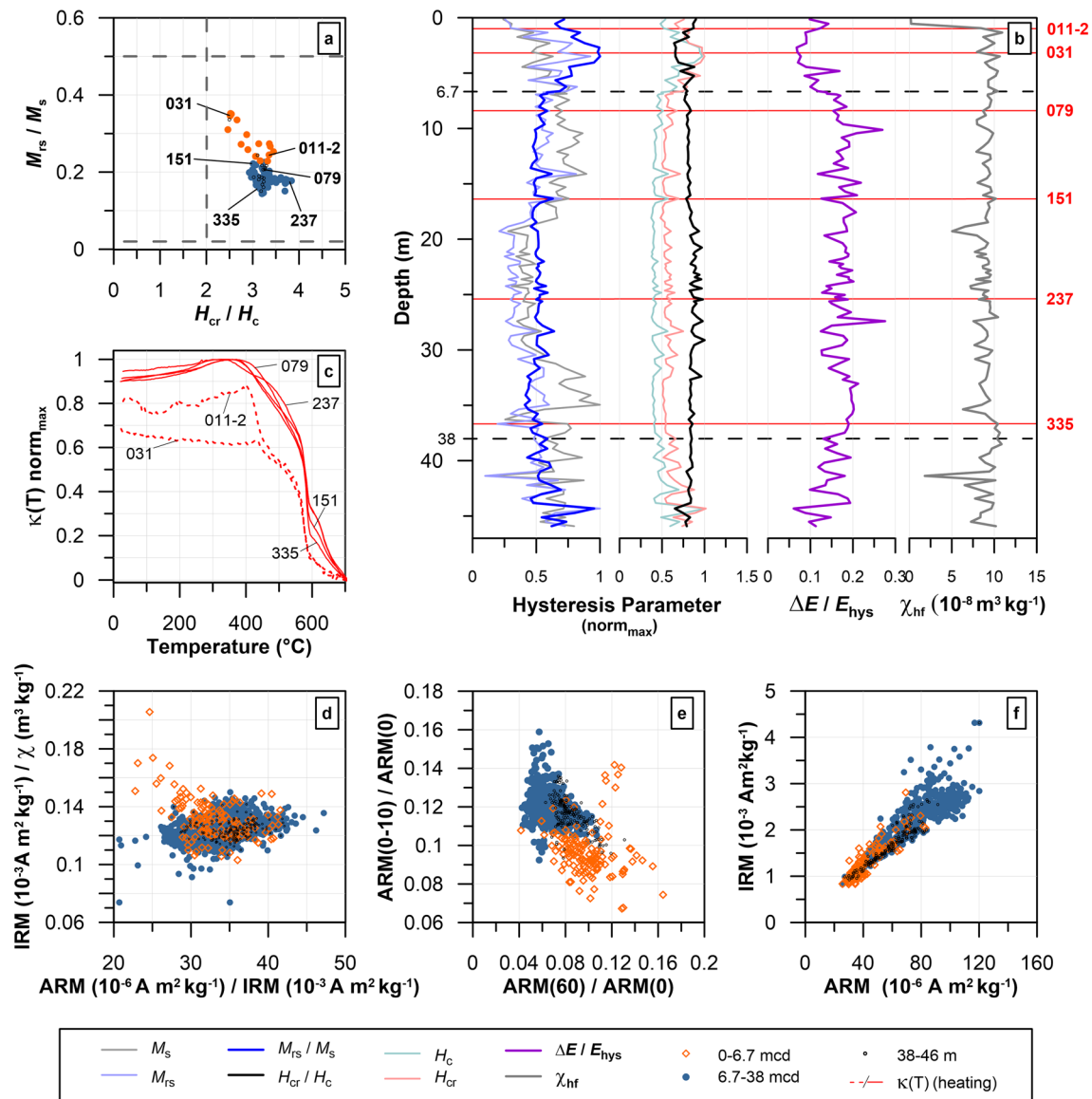


**Figure 3.** Biplots and downcore graphs visualizing mineral magnetic properties using VSM (a), (b), Kappabridge (c), and cryogenic magnetometer (d)-(f) data. (a) Hysteresis parameters in the Day plot. (b) Downcore variations.  $M_s$ ,  $M_{rs}$ ,  $M_{rs}/M_s$ ,  $H_c$ ,  $H_{cr}$ , and  $H_{cr}/H_c$  normalized to the respective maximum.  $\Delta E/E_{hys}$  and  $\chi_{hf}$  in absolute numbers. (c) Heating curves of  $\kappa(T)$ . (d) Biplot of grain-size indicators. (e) Plot of anhysteretic remanent magnetization (ARM) fraction remaining after 60 mT demagnetization versus ARM fraction demagnetized below 10 mT. (f) Isothermal remanent magnetization versus ARM.

wedge-shaped final section of the heating curve points towards thermally induced conversion of magnetite via maghemite to hematite. The drop at  $\sim 400^\circ\text{C}$  visible at samples 011-2 and 031 is attributed to the decomposition of greigite (Minyuk et al., 2013) and leads to the exceeding of the cooling curve over the heating curve by neoformation of magnetite and maghemite (Figure S2). While the magneto mineralogy and grain-sizes appear consistent, the concentration of the magnetic fraction varies between 38 and  $\sim 6.7$  mcd, as documented by  $M_{rs}$  and  $M_s$  (Figure 3b), and by  $\chi$ , ARM, and IRM (Figure 2). Variations in the relative concentration of magnetic minerals might be caused by different sediment sources, or by a sorting effect. Different lithogenic sources, in particular basalts and sandstones from the catchment (Text S6 and Figure S2), would be characterized by contrasting values of the  $\chi_{hf}$ , which represent the para- and diamagnetic mineral fraction. The nearly constant  $\chi_{hf}$  values thus, point to changes in the selective transport of magnetic minerals. For samples from the upper  $\sim 6.7$  mcd, a refinement of magnetic particles is indicated by the Day plot (Figure 3a) and by a significant decrease in  $\Delta E/E_{hys}$  (Figure 3b). Additionally, hysteresis parameters

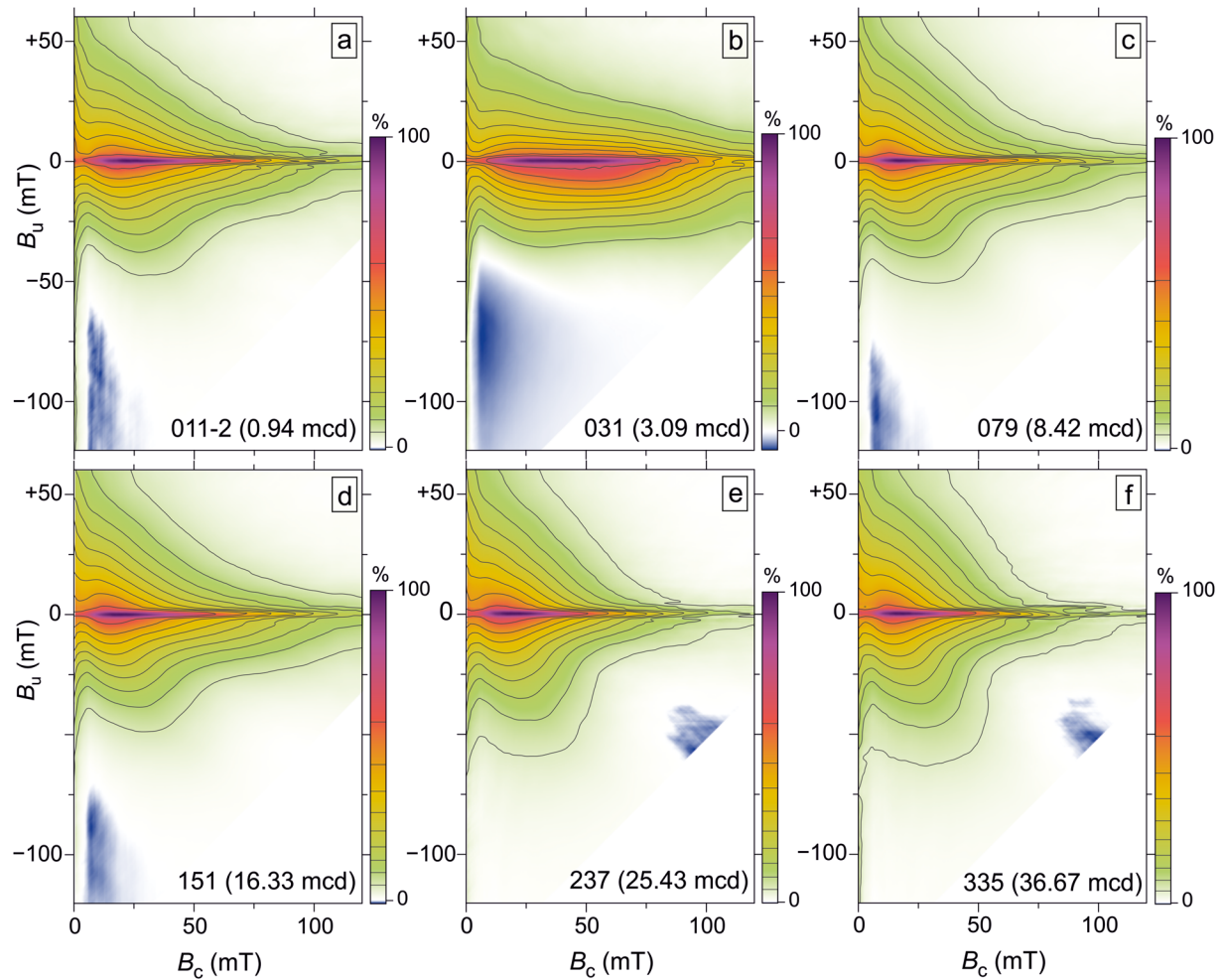


**Figure 4.** High-resolution first-order reversal curve (FORC) diagrams. (a)–(f) Contour lines represent the 10%, 20%, 30%, 40%, 50%, 60%, 70%, 80%, and 90% quantiles of the total FORC magnetization. The area enclosed between two successive contour levels thus represents 10% of the total FORC magnetization.

are highly variable. This change in magnetic properties, might be caused by different sources of magnetic minerals or by diagenetic overprinting. Notwithstanding these differences, bulk rock magnetic parameters point systematically to the PSD size range for ferrimagnetic mineral fractions throughout the core (Figure 3d). Only few samples are characterized by elevated  $IRM/\chi$  values typical for smaller particles and/or the iron sulfide greigite (Roberts et al., 1996). Biplots in Figures 3e and 3f support the above conclusions. In particular, Figure 3e indicates that the remanence carriers of the upper section are magnetically harder than those from below.

FORC diagrams confirm the findings deduced from bulk magnetic parameters and provide a more specific insight into subtle changes in magnetic grain-size and mineralogy (Figure 4). All diagrams are dominated by a typical PSD signature, given by contour lines that diverge almost linearly towards  $B_c = 0$  and by a small indent of low-amplitude contours over the lower quadrant (Egli & Winklhofer, 2014; Lascu et al., 2018; Muxworthy & Dunlop, 2002; Roberts et al., 2000). In accordance with  $\Delta E/E_{\text{hys}}$ , the increase of the vertical spread, the shift of the central peak towards lower  $B_c$  values, and the appearance of a negative region in the lower quadrant around  $B_c = 100$  mT indicate a slightly coarser magnetic grain-size of samples shown in Figures 4e and 4f compared to the other FORC diagrams. In addition to the PSD signature with a coercivity range consistent to magnetite, all diagrams contain a central ridge, which is typical for non-interacting SD particles, or isolated chains of such particles from fossil remains of magnetotactic bacteria (magnetofossils) (Egli et al., 2010). The existence of such SD particles is also confirmed by the negative FORC amplitudes in the lower quadrant near  $B_c = 0$ . These negative amplitudes are caused by the reversible rotation of SD

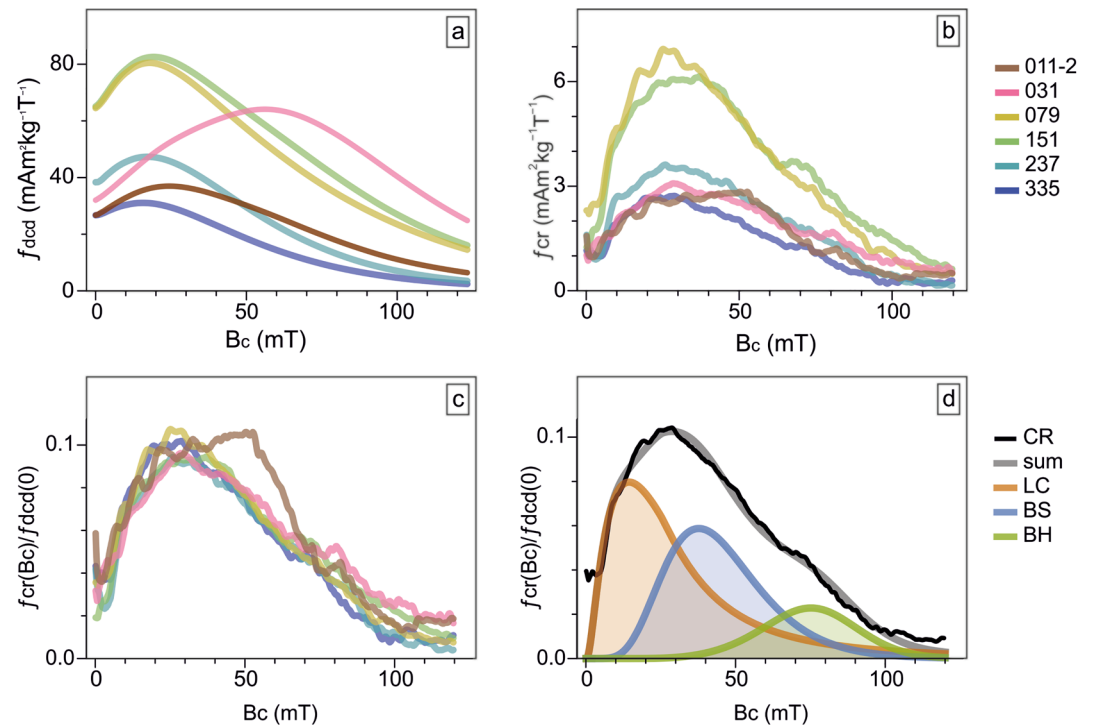


**Figure 5.** Coercivity distributions of first-order reversal curve (FORC) diagrams. (a) Coercivity distributions  $f_{dcd}$  obtained from DC demagnetization curve data contained in the FORC measurements. (b) Central ridge coercivity distributions  $f_{cr}$ . Localized peaks for sample 011-2 at  $\sim 50$  mT and sample 151 at  $\sim 70$  mT are probably associated with correlated measurement noise. (c) Same as (b) after normalizing  $f_{cr}$  with  $f_{dcd}(0)$ . (d) Coercivity analysis of the  $f_{cr}$  stack obtained with samples 079 and 335. The legend of (a)–(c), and (d) are next to (b) and (d), respectively.

magnetic moments in the applied field (Newell, 2005). The contribution of the central ridge to the bulk magnetization, obtained by integrating the isolated ridge over  $B_c$  and  $B_u$ , is comprised  $\sim 3\%$ – $8\%$  of  $M_{rs}$ . Much larger relative contributions, often exceeding 50%, are observed in magnetofossil-rich sediments (Ludwig et al., 2013). Few terms of comparison are available for lithogenic SD particles: the central ridge of SD magnetite contained in silicate host minerals has been shown to contribute to  $\sim 3\%$  of  $M_{rs}$  in pelagic carbonates from the Pacific Ocean (Ludwig et al., 2013).

The FORC signature of Co1401-031 ( $\sim 3$  mcd) is clearly distinct from that of the other examples (Figure 4b); contours are more oval-shaped, the central ridge peak is shifted towards higher coercivities, and the negative contribution associated with SD particles is much more pronounced. This is a typical signature of greigite-bearing sediments (Egli et al., 2010; Roberts, et al., 2011; Rowan & Roberts, 2006; Vasiliev et al., 2008). In this case, it is superimposed with the PSD signature of lithogenic minerals, recognizable from the low-amplitude contours in the upper quadrant. Greigite is a byproduct of reductive diagenesis, which leads to the dissolution of ultrafine magnetite particles, including those contributing to the central ridge (Rowan & Roberts, 2006). The coexistence of greigite and SD magnetite in lake sediments suggests that the dissolution of SD magnetite was incomplete (Egli, 2004a, 2004b). It is also possible that greigite magnetofossils contribute to the central ridge (Chen et al., 2014).

Further insight into the nature of the SD and PSD signatures in the FORC diagrams are provided by coercivity distributions. Figure 5a shows the coercivity distributions  $f_{dcd}$  obtained from DC demagnetization curves in a subset of FORC measurements. These coercivity distributions have different amplitudes that reflect concentration changes. The peak of sample 031 at  $\sim 60$  mT is typical of greigite-bearing sediments. The intermediate shape of sample 011-2 might be explained by a minor greigite contribution that is not easily identifiable in the corresponding FORC diagram. A coercivity analysis of  $f_{dcd}$  is not possible because all curves are truncated at  $\sim 125$  mT, far from saturation. However, potential high-coercivity components are of minor importance since they are not present in sufficient quantity to significantly affect the hysteresis data.

The downcore shift of the  $f_{\text{dcd}}$  peak towards lower coercivities, from  $\sim 20$  to  $\sim 15$  mT confirms the grain-size trend observed in the FORC diagrams. The coercivity distributions  $f_{\text{cr}}$  associated with the central ridge (Figure 5b) share a similar shape, which is distinct from that of  $f_{\text{dcd}}$ , up to sample 011-2, which might be affected by a larger amount of noise. All  $f_{\text{cr}}$  distributions collapse onto a single curve when normalized by  $f_{\text{dcd}}(0)$  (Figure 5c), but not by other normalizations (e.g.,  $M_{\text{rs}}$  or  $M_{\text{s}}$ ). This means that the central ridge magnetization (Table S2) does not correlate with  $M_{\text{rs}}$  ( $M_{\text{cr}}/M_{\text{rs}}$ :  $\sim 3\%$ – $8\%$ ),  $\chi_{\text{hf}}$  ( $M_{\text{cr}}/\chi_{\text{hf}}$ :  $\sim 3$ – $6$  T $^{-1}$ ) or  $M_{\text{s}}$  ( $M_{\text{cr}}/M_{\text{s}}$ :  $\sim 1.0\%$ – $1.6\%$ ), as expected from a source that is independent from the detrital input. The good correlation between  $M_{\text{cr}}$  and the contribution  $f_{\text{dcd}}(0)$  of the backfield distribution at  $H = 0$  (Figure 5c) is probably due to the causal cancellation of concentration and grain-size trends affecting  $f_{\text{dcd}}(0)$ .

The central ridge distributions of samples 079 and 335 were of sufficient quality and similarity to stack them and perform a coercivity analysis (Figure 5d). Because  $f_{\text{cr}}$  is entirely controlled by non-interacting SD particles or isolated chains of such particles (Egli et al., 2010), it was fitted by a linear combination of coercivity components attributed to SD particles with large ARM/IRM ratios in Egli (2004a). The low-coercivity component LC corresponds to the components D and EX in Egli (2004a), which have been associated with well-dispersed, nearly equidimensional magnetite particles of pedogenic or diagenetic origin. The components BS and BH, on the other hand, are exclusively associated with magnetofossil-rich sediments and have been interpreted as originating from chains of equidimensional (BS) and elongated (BH) magnetosomes (Egli, 2004a, 2004b; Heslop et al., 2014). The existence of the component BH, which appears exclusive of magnetite magnetofossils (Chen et al., 2014) excludes significant reductive dissolution of biogenic and detrital magnetite particles. The lower magnetofossil concentration of  $0.2$ – $0.4$  mA m $^2$  kg $^{-1}$  compared to  $2.2$  mA m $^2$  kg $^{-1}$  in a magnetofossil-rich pelagic carbonate (Ludwig et al., 2013) can be explained by a dilution effect due to the much higher sedimentation rates. This assumes that the growth of magnetotactic bacteria is limited by the supply of organic material and not by iron. Since the sediment is low in organic material, it is reasonable to assume that this is the limiting factor.

#### 4. Conclusions

We have characterized the mineral magnetic properties of the 46-m-long core Co1401 from Levinson-Lessing Lake in northern Siberia. Because of core disturbances, only the top 38 mcd were usable for analyses. However, above 38 mcd, Co1401 is characterized by an exceptionally homogeneous magnetic mineralogy, especially between 6.7 and 38 mcd. The main remanence carrier is PSD magnetite,  $\sim 5$   $\mu\text{m}$  in size or less, complemented by SD particles (up to 8%), probably mainly of biogenic origin. The contribution of MD particles, if existing, is generally low. Magnetic mineral analyses suggest a division of samples from above and below 6.7 mcd. Above  $\sim 6.7$  mcd, the bulk magnetic mineralogy is harder and the bulk magnetic grain-size decreases. Greigite is present between  $\sim 1$  and 5 mcd, indicating reductive conditions. However, the persistence of a central ridge in a sample from  $\sim 3$  mcd, where the greigite concentration is maximal, excludes the onset of reductive magnetite dissolution.

The homogeneous magnetic mineralogy carried dominantly by particles in PSD state, combined with the reported high sedimentation rates represent ideal prerequisites for paleomagnetic studies. A comparable study site that enable to obtain a reliable and high-resolution record of the EMFs changes is not available in the Eurasian Arctic within a radius of more than 1,500 km. Besides, we illustrate the high potential of core Co1401 for a multi-proxy approach to decipher the climatic and environmental conditions in the vicinity of Levinson-Lessing Lake.

#### Data Availability Statement

Datasets for this research are available in Scheidt et al. (2021).

#### Acknowledgments

This study was funded by the German Federal Ministry for Education and Research (project PLOT: Paleolimnological Transect, grant nos. 03G0859A and 03F0830A).

#### References

- Andreev, A. A., Tarasov, P. E., Siebert, C., Ebel, T., Klimanov, V. A., Melles, M., et al. (2003). Late Pleistocene and Holocene vegetation and climate on the northern Taymyr Peninsula, Arctic Russia. *Boreas*, 32(3), 484–505. <https://doi.org/10.1111/j.1502-3885.2003.tb01230.x>  
[x10.1080/03009480310003388](https://doi.org/10.1080/03009480310003388)



- Chen, A. P., Berounsky, V. M., Chan, M. K., Blackford, M. G., Cady, C., Moskowitz, B. M., et al. (2014). Magnetic properties of uncultivated magnetotactic bacteria and their contribution to a stratified estuary iron cycle. *Nature Communications*, 5(1), 4797. <https://doi.org/10.1038/ncomms5797>
- Day, R., Fuller, M., & Schmidt, V. A. (1977). Hysteresis properties of titanomagnetites: Grain-size and compositional dependence. *Physics of the Earth and Planetary Interiors*, 13(4), 260–267. [https://doi.org/10.1016/0031-9201\(77\)90108-x](https://doi.org/10.1016/0031-9201(77)90108-x)
- Ebel, T., M. Melles, & F. Niessen, (1999). Laminated Sediments from Levinson-Lessing Lake, Northern Central Siberia - A 30,000 Year Record of Environmental History? In *Land-ocean systems in the siberian arctic*, edited, pp. 425–435, Springer, Berlin, Heidelberg. [https://doi.org/10.1007/978-3-642-60134-7\\_34](https://doi.org/10.1007/978-3-642-60134-7_34)
- Egli, R. (2004a). Characterization of individual rock magnetic components by analysis of remanence curves. 1. Unmixing natural sediments. *Studia Geophysica et Geodaetica*, 48(2), 391–446. <https://doi.org/10.1016/j.pce.2004.04.00110.1023/b:sgseg.0000020839.45304.6d>
- Egli, R. (2004b). Characterization of individual rock magnetic components by analysis of remanence curves. 3. Bacterial magnetite and natural processes in lakes. *Physics and Chemistry of the Earth, Parts A/B/C*, 29(13), 869–884. <https://doi.org/10.1016/j.pce.2004.03.010>
- Egli, R. (2013). VARIFORC: An optimized protocol for calculating non-regular first-order reversal curve (FORC) diagrams. *Global and Planetary Change*, 110, 302–320. <https://doi.org/10.1016/j.gloplacha.2013.08.003>
- Egli, R., Chen, A. P., Winklhofer, M., Kodama, K. P., & Horng, C.-S. (2010). Detection of noninteracting single domain particles using first-order reversal curve diagrams. *Geochemistry, Geophysics, Geosystems*, 11(1), Q01Z11. <https://doi.org/10.1029/2009GC002916>
- Egli, R., & Winklhofer, M. (2014). Recent developments on processing and interpretation aspects of first-order reversal curves (forc). *Ученые записки Казанского университета. Серия Естественные науки (Proceedings of Kazan University)*, 156(1), 14–53.
- Fabian, K. (2003). Some additional parameters to estimate domain state from isothermal magnetization measurements. *Earth and Planetary Science Letters*, 213(3–4), 337–345. [https://doi.org/10.1016/S0012-821X\(03\)00329-7](https://doi.org/10.1016/S0012-821X(03)00329-7)
- Fabian, K. (2006). Approach to saturation analysis of hysteresis measurements in rock magnetism and evidence for stress dominated magnetic anisotropy in young mid-ocean ridge basalt. *Physics of the Earth and Planetary Interiors*, 154(3–4), 299–307. <https://doi.org/10.1016/j.pepi.2005.06.016>
- Gehring, A. U., Fischer, H., Louvel, M., Kunze, K., & Weidler, P. G. (2009). High temperature stability of natural maghemite: A magnetic and spectroscopic study. *Geophysical Journal International*, 179(3), 1361–1371. <https://doi.org/10.1111/j.1365-246X.2009.04348.x>
- Heslop, D., Roberts, A. P., & Chang, L. (2014). Characterizing magnetofossils from first-order reversal curve (FORC) central ridge signatures. *Geochemistry, Geophysics, Geosystems*, 15(6), 2170–2179. <https://doi.org/10.1002/2014gc005291>
- Lascu, I., Einsle, J. F., Ball, M. R., & Harrison, R. J. (2018). The Vortex state in geologic materials: A micromagnetic perspective. *Journal of Geophysical Research: Solid Earth*, 123(9), 7285–7304. <https://doi.org/10.1029/2018JB015909>
- Lebas, E., Krastel, S., Wagner, B., Gromig, R., Fedorov, G., Baumer, M., et al. (2019). Seismic stratigraphical record of Lake Levinson-Lessing, Taymyr Peninsula: Evidence for ice-sheet dynamics and lake-level fluctuations since the Early Weichselian. *Boreas*, 48(2), 470–487. <https://doi.org/10.1111/bor.12381>
- Liu, X., Shaw, J., Jiang, J., Bloemendal, J., Hesse, P., Rolph, T., & Mao, X. (2010). Analysis on variety and characteristics of maghemite. *Science China Earth Sciences*, 53(8), 1153–1162. <https://doi.org/10.1007/s11430-010-0030-2>
- Ludwig, P., Egli, R., Bishop, S., Chernenko, V., Frederichs, T., Rugel, G., et al. (2013). Characterization of primary and secondary magnetite in marine sediment by combining chemical and magnetic unmixing techniques. *Global and Planetary Change*, 110, 321–339. <https://doi.org/10.1016/j.gloplacha.2013.08.018>
- Minyuk, P. S., Tyukova, E. E., Subbotnikova, T. V., Kazansky, A. Y., & Fedotov, A. P. (2013). Thermal magnetic susceptibility data on natural iron sulfides of northeastern Russia. *Russian Geology and Geophysics*, 54(4), 464–474. <https://doi.org/10.1016/j.rgg.2013.03.008>
- Muxworthy, A. R., & Dunlop, D. J. (2002). First-order reversal curve (FORC) diagrams for pseudo-single-domain magnetites at high temperature. *Earth and Planetary Science Letters*, 203(1), 369–382. [https://doi.org/10.1016/S0012-821X\(02\)00880-4](https://doi.org/10.1016/S0012-821X(02)00880-4)
- Newell, A. J. (2005). A high-precision model of first-order reversal curve (FORC) functions for single-domain ferromagnets with uniaxial anisotropy. *Geochemistry, Geophysics, Geosystems*, 6(5), Q05010. <https://doi.org/10.1029/2004GC000877>
- Niessen, F., Ebel, T., Kopsch, C., & Fedorov, G. B. (1999). High-resolution seismic stratigraphy of lake sediments on the Taymyr Peninsula, Central Siberia. In H. Kassens, H. A. Bauch, I. A. Dmitrenko, H. Eicken, H.-W. Hubberten, M. Melles, J. Thiede, & L. A. Timokhov (Eds.), *Land-ocean systems in the Siberian arctic: Dynamics and history* (pp. 437–456). Berlin, Heidelberg: Springer Berlin Heidelberg. [https://doi.org/10.1007/978-3-642-60134-7\\_35](https://doi.org/10.1007/978-3-642-60134-7_35)
- Nishitani, T., & Kono, M. (1983). Curie temperature and lattice constant of oxidized titanomagnetite. *Geophysical Journal International*, 74(2), 585–600. <https://doi.org/10.1111/j.1365-246X.1983.tb01890.x>
- Pike, C. R., Roberts, A. P., & Verosub, K. L. (1999). Characterizing interactions in fine magnetic particle systems using first order reversal curves. *Journal of Applied Physics*, 85(9), 6660–6667. <https://doi.org/10.1063/1.370176>
- Roberts, A. P., Chang, L., Rowan, C. J., Horng, C.-S., & Florindo, F. (2011). Magnetic properties of sedimentary greigite (Fe<sub>3</sub>S<sub>4</sub>): An update. *Reviews of Geophysics*, 49(1), RG1002. <https://doi.org/10.1029/2010RG000336>
- Roberts, A. P., Pike, C. R., & Verosub, K. L. (2000). First-order reversal curve diagrams: A new tool for characterizing the magnetic properties of natural samples. *Journal of Geophysical Research*, 105(B12), 28461–28475. <https://doi.org/10.1029/2000jb900326>
- Roberts, A. P., Reynolds, R. L., Verosub, K. L., & Adam, D. P. (1996). Environmental magnetic implications of Greigite (Fe<sub>3</sub>S<sub>4</sub>) formation in a 3 m.y. lake sediment record from Butte Valley, northern California. *Geophysical Research Letters*, 23(20), 2859–2862. <https://doi.org/10.1029/96GL02831>
- Rowan, C. J., & Roberts, A. P. (2006). Magnetite dissolution, diachronous greigite formation, and secondary magnetizations from pyrite oxidation: Unraveling complex magnetizations in Neogene marine sediments from New Zealand. *Earth and Planetary Science Letters*, 241(1), 119–137. <https://doi.org/10.1016/j.epsl.2005.10.017>
- Scheidt, S., Egli, R., Rolf, C., & Melles, M. (2021). *Magnetic characterization and paleomagnetic analyses of lacustrine sediments from Levinson-Lessing Lake, Siberia*. <https://doi.org/10.6084/m9.figshare.c.5369129.v1>
- St-Onge, G., & Stoner, J. (2011). Paleomagnetism near the North magnetic pole: A unique vantage point for understanding the dynamics of the geomagnetic field and its secular variations. *Oceanography*, 24(3), 42–50. <https://doi.org/10.5670/oceanog.2011.53>
- Vasiliev, I., Franke, C., Meeldijk, J. D., Dekkers, M. J., Langereis, C. G., & Krijgsman, W. (2008). Putative greigite magnetofossils from the pliocene epoch. *Nature Geoscience*, 1(11), 782–786. <https://doi.org/10.1038/ngeo335>
- Wiers, S., Snowball, I., O'Regan, M., & Almqvist, B. (2019). Late pleistocene chronology of sediments from the yermak plateau and uncertainty in dating based on geomagnetic excursions. *Geochemistry, Geophysics, Geosystems*, 20(7), 3289–3310. <https://doi.org/10.1029/2018GC007920>
- Wiers, S., Snowball, I., O'Regan, M., Pearce, C., & Almqvist, B. (2020). The Arctic ocean manganese cycle, an overlooked mechanism in the anomalous palaeomagnetic sedimentary record. *Frontiers of Earth Science*, 8(75). <https://doi.org/10.3389/feart.2020.00075>

## References From the Supporting Information

- Anisimov, M. A., & Pospelov, I. N. (1999). The landscape and geobotanical characteristics of the Levinson- Lessing Lake basin, Byrranga mountains, Central Taimyr, in *Land-ocean systems in the siberian arctic*, edited, pp. 307–327, Springer. [https://doi.org/10.1007/978-3-642-60134-7\\_27](https://doi.org/10.1007/978-3-642-60134-7_27)
- Bolshiyarov, D. Y., & Anisimov, M. (1995). Investigations in the Levinson-Lessing Lake area. Geomorphological studies and landscape mapping. Russian–German cooperation: The expedition Taymyr 1994. *Berichte zur Polarforschung*, 175, 9–13
- Gromov, P., Proskurinin, V., & Schneider, G. (2014). *Geological map of the Taymyr Peninsula*. <https://doi.org/10.2172/1121044>. <http://webmapget.vsegei.ru/index.html>
- Torsvik, T. H., & Andersen, T. B. (2002). The Taimyr fold belt, Arctic Siberia: Timing of prefold remagnetization and regional tectonics. *Tectonophysics*, 352(3), 335–348. [https://doi.org/10.1016/S0040-1951\(02\)00274-3](https://doi.org/10.1016/S0040-1951(02)00274-3)
- Walderhaug, H. J., Eide, E. A., Scott, R. A., Inger, S., & Golionko, E. G. (2005). Palaeomagnetism and  $^{40}\text{Ar}/^{39}\text{Ar}$  geochronology from the South Taimyr igneous complex, Arctic Russia: A middle-late triassic magmatic pulse after Siberian flood-basalt volcanism. *Geophysical Journal International*, 163(2), 501–517. <https://doi.org/10.1111/j.1365-246X.2005.02741.x>